

# Current response to axial gauge fields in noncentrosymmetric magnetic Weyl semimetals

Long Liang

Department of Physics, Institute of Solid State Physics and Center for Computational Sciences, Sichuan Normal University, Chengdu, Sichuan 610066, China

We investigate the electric current response to axial gauge fields in noncentrosymmetric magnetic Weyl semimetals. The absence of both time-reversal and inversion symmetries allows for new types of responses. We systematically calculate the transverse, longitudinal, and Hall responses to axial gauge potentials with both linear and quadratic dispersion relations. The transverse and Hall responses are of comparable magnitude, while the longitudinal response is much smaller. Notably, with increasing frequency, the transverse and Hall response functions manifest a peak whose height is determined by the properties of Weyl fermions and is independent of the axial gauge potential. The main features of the response functions survive in the presence of disorders. As applications of our results, we propose a Hall type magnetopiezoelectric effect, where a transverse sound wave can induce an electric current whose direction is perpendicular to the directions of sound propagation and polarization. Our results also provide a mechanism to excite magnons using electric fields and could be useful for magnon spintronics.

*Introduction.*— In recent years, there has been a surge of interest in topological quantum matter with gapless nodes and linear dispersion relation around the nodes. Typical materials include Dirac and Weyl semimetals and their generalizations [1, 2]. The nodal degrees of freedom in these materials allow for the realization of responses that go beyond the conventional light-matter interaction paradigm [3, 4]. In particular, axial gauge fields, which are out of phase motion of the nodes, can be manipulated through various methods such as optical [5], electrical [6], magnetic, and mechanical [7–10]. Indeed, besides the response to electromagnetic fields [11–21], the response of topological semimetals to axial gauge fields has also attracted much attention and various novel phenomena [22–35] have been proposed.

Noncentrosymmetric magnetic Weyl semimetals that break both symmetries have been proposed in a number of materials such as Huesler magnets like  $\text{Ti}_2\text{MnX}$  ( $X=\text{Al, Ga, or In}$ ) [36, 37] and  $\text{InMnTi}_2$  [38], and the rare earth family of compounds  $R\text{AlX}$  where  $R$ =rare earth and  $X=\text{Ge or Si}$  [39].

Recently, several candidate materials in the rare earth family have been experimentally identified [40–45]. Motivated by these experimental discoveries, in this work, we study the electric current response to axial gauge fields in noncentrosymmetric magnetic Weyl semimetals, where the absence of both time-reversal and inversion symmetries paves the way for new types of responses, which are otherwise forbidden in Weyl semimetals break only inversion or time-reversal symmetry. In particular, to generate electric currents, the external perturbations need not break inversion nor time-reversal.

We systematically calculate the diagonal longitudinal and transverse response functions as well as the off-diagonal Hall type response function. We consider both linear (e.g., sound wave) and quadratic dispersion (e.g., ferromagnetic spin wave) relations of external perturbations. The frequency dependence of the response functions is obtained. We find that the transverse and Hall

type responses are of comparable magnitude, while the longitudinal one is substantially smaller. Moreover, the momentum dependence of the axial gauge potential results in a peak in the response functions. For the transverse and Hall responses, the height of the peak is independent of external perturbations. As applications of our results, we predict a Hall type magnetopiezoelectric effect [46–49], and also propose a possible mechanism of magnon electric field interconversion.

*Model.*— To elucidate the essential features of the response to axial gauge potentials, we employ a minimal two band model of a Weyl semimetal that breaks both time-reversal and inversion symmetries. The corresponding Hamiltonian is  $H = H_+ \oplus H_-$  with

$$H_\lambda = \hbar v_F \lambda (\mathbf{k} - \lambda \mathbf{b}) \cdot \boldsymbol{\sigma} + \lambda b_0 \sigma^0, \quad (1)$$

where  $\lambda = \pm 1$  denotes the chirality of the Weyl nodes,  $\hbar$  is the reduced Planck's constant,  $v_F$  is the Fermi velocity,  $\sigma_i$  with  $i = 1, 2, 3$  are the three Pauli matrices,  $\sigma^0$  is the two dimensional identity matrix,  $2\mathbf{b}$  and  $2b_0$  are the separations of the two Weyl nodes in momentum and energy, respectively. The inversion symmetry is broken by nonzero  $b_0$ , while  $\mathbf{b} \neq 0$  breaks the time-reversal symmetry. In the following, the Fermi velocity, reduced Planck's constant, Boltzmann constant, and electric charge are taken to be unity and will be recovered when necessary.

In the low energy limit, the effects of external perturbations can be captured by axial gauge potentials [3, 4]. This provides a general way to investigate the current response to external perturbations. The electric current induced by the scalar axial gauge potential has been explored previously [35]. We thus focus on the effect of vector axial gauge potential  $\mathbf{A}_5$ . Using the linear response theory, the electric current induced by the axial vector potential is given by  $j_i(\omega, \mathbf{p}) = \Pi_{ij}(\omega, \mathbf{p}) A_{5,j}(\omega, \mathbf{p})$ . We calculate the retarded current-axial current response function  $\Pi_{ij}(\omega, \mathbf{p})$  by utilizing the imaginary time formalism,  $\Pi_{ij}(i\nu_m, \mathbf{p}) = \frac{1}{\beta} \sum_k \text{tr}[\hat{j}_i G(k+q) \hat{j}_j \gamma_5 G(k)]$ , where

$\beta$  is the inverse temperature,  $k \equiv (i\omega_n, \mathbf{k})$ ,  $\omega_n = (2n+1)\pi/\beta$  is the fermionic Matsubara frequency, and  $\nu_m = 2m\pi/\beta$  is the bosonic one. The current operator is given by  $\hat{j}_i = \partial_{k_i} H(\mathbf{k} + \mathbf{q}/2) = \sigma_i \oplus -\sigma_i$ , and  $\gamma_5 = I \oplus -I$  is the fifth gamma matrix. The Matsubara Green's function is given by  $G(i\omega_n, \mathbf{k}) = [i\omega_n - H(\mathbf{k}) - \mu]^{-1}$ , with  $\mu$  being the chemical potential. In the following we assume  $\mu > 0$ .

*Response function.*— Now we calculate the response function. Performing Matsubara frequency summation and analytical continuation,  $i\nu_m \rightarrow \omega + i0^+$ , we obtain

$$N_{ij}^{\lambda ss'}(\mathbf{k}, \mathbf{p}) = \frac{1}{2} \left[ \left( 1 - ss' \frac{\mathbf{k}^\lambda \cdot (\mathbf{k}^\lambda + \mathbf{p})}{|\mathbf{k}^\lambda| |\mathbf{k}^\lambda + \mathbf{p}|} \right) \delta_{ij} + ss' \frac{k_i^\lambda (k_j^\lambda + p_j) + k_j^\lambda (k_i^\lambda + p_i)}{|\mathbf{k}^\lambda| |\mathbf{k}^\lambda + \mathbf{p}|} + i\epsilon_{ijl} \left( s' \frac{k_l^\lambda}{|\mathbf{k}^\lambda|} - s \frac{k_l^\lambda + p_l}{|\mathbf{k}^\lambda + \mathbf{p}|} \right) \right], \quad (3)$$

with  $\mathbf{k}^\lambda = \mathbf{k} - \lambda \mathbf{b}$  and  $\epsilon_{ijl}$  being the totally antisymmetric tensor. The  $s = s'$  and  $s \neq s'$  terms correspond to intraband and interband transitions, respectively.

The first two terms in Eq. (3) are symmetric in  $i$  and  $j$ , while the third term is antisymmetric. The response function is a second order tensor constructed from  $\mathbf{p}$  and  $\epsilon_{ijk}$ , so it must take the form  $\Pi_{ij}(\omega, \mathbf{p}) = \Pi_T(\omega, p)(\delta_{ij} -$

the retarded response function  $\Pi_{ij}(\omega, \mathbf{p})$ ,

$$\Pi_{ij}(\omega, \mathbf{p}) = \sum_{\mathbf{k}, \lambda, s, s'} \frac{N_{ij}^{\lambda ss'}(\mathbf{k}, \mathbf{p}) [f(\epsilon_{s, \mathbf{k}+\mathbf{p}}^\lambda) - f(\epsilon_{s', \mathbf{k}}^\lambda)]}{\omega + \epsilon_{s', \mathbf{k}}^\lambda - \epsilon_{s, \mathbf{k}+\mathbf{p}}^\lambda + i0^+}, \quad (2)$$

where  $\epsilon_{s, \mathbf{k}}^\lambda = s|\mathbf{k} - \lambda \mathbf{b}| + \lambda b_0$  with  $s = \pm 1$  denotes the particle and hole bands,  $f(\epsilon) = 1/(e^{\beta(\epsilon - \mu)} + 1)$  is the Fermi-Dirac distribution function. In this work we focus on the zero temperature limit. The transition amplitude  $N_{ij}^{\lambda ss'}(\mathbf{k}, \mathbf{p})$  is given by

$p_i p_j / p^2) + \Pi_L(\omega, p) p_i p_j / p^2 + \Pi_H(\omega, p) \epsilon_{ijk} p_k / p$ . Here  $\Pi_T(\omega, p)$  is the transverse response function,  $\Pi_L(\omega, p)$  is the longitudinal one, and  $\Pi_H(\omega, p)$  describes a Hall-type response.

*Longitudinal and transverse responses.*— We first consider the longitudinal and transverse response functions. It is convenient to first calculate their imaginary parts,

$$\text{Im} \Pi_{L/T}^{\text{intra}}(\omega, p) = \sum_{\lambda} \lambda \theta(p - |\omega|) \theta(2|\mu_\lambda| + \omega - p) g_{L/T} F_{L/T}(-\omega, |\mu_\lambda|, p) - (\omega \rightarrow -\omega), \quad (4)$$

$$\text{Im} \Pi_{L/T}^{\text{inter}}(\omega, p) = \sum_{\lambda} \lambda \theta(|\omega| - p) g_{L/T} \left[ \theta(p - |\omega - 2\mu_\lambda|) F_{L/T}(\omega, \mu_\lambda, p) + \frac{\theta(\omega - 2\mu_\lambda - p)}{24\pi} \right] - (\omega \rightarrow -\omega), \quad (5)$$

where  $\theta(x)$  is the step function,  $\mu_\lambda = \mu + \lambda b_0$ ,  $g_L = \omega^2$ ,  $g_T = \omega^2 - p^2$ ,  $F_L(\omega, \mu, p) = \omega^2 (2\mu - \omega - p)^2 (2\mu + 2p - \omega) / (96\pi p^3)$ , and  $F_T = (\omega + p - 2\mu)[(2\mu - \omega)(2\mu - \omega + p) + 4p^2] / (192\pi p^3)$ . It is clear that if  $|\omega| < v_F p$  (here we recover the Fermi velocity), only the intraband term is nonzero, while the interband processes contribute in the opposite limit. The imaginary parts of the longitudinal and transverse response functions are odd in frequency, which implies that their real counterparts are even functions. In the following we only consider the  $\omega > 0$  region unless otherwise stated.

The dispersion relation of the axial gauge field depends on its physical origin. For example, for sound waves and antiferromagnetic spin waves,  $\omega = v_s p$  in the low energy limit, where  $v_s$  is the sound or spin wave velocity. The low energy dispersion relation for ferromagnetic spin waves is  $\omega = D p^2$ , with  $D$  being the spin stiffness. For helical magnetic order observed in Weyl semimetals [41–43], the magnon dispersion is highly anisotropic [50]. In real materials, we typically have  $\alpha \equiv v_s / v_F \ll 1$  and  $\gamma \equiv D k_F / v_F \ll 1$  ( $k_F$  is the Fermi momentum) [51]. In the following we study both the linear and quadratic

dispersions of the axial gauge potential and focus on the  $\alpha \ll 1$  and  $\gamma \ll 1$  regimes. Fig. 1 shows the imaginary parts of the longitudinal and transverse responses functions for both linear and quadratic dispersions as functions of frequency. The step-like feature can be observed, and one can also see that the transverse response is much larger than the longitudinal one. In the linear dispersion case [Fig. 1(a) and (b)], the interband term Eq. (5) vanishes identically since  $v_F / v_s > 1$ . For the quadratic dispersion case [Fig. 1(c) and (d)], the interband contribution also vanishes in the plotted frequency region.

The real parts of the response functions are obtained through the Kramers-Kronig relation from the imaginary parts. Fig. 2 shows the real parts of the response functions with the same parameters as in Fig. 1. For the linear dispersion case, the real part of the longitudinal response function decreases monotonically with the increasing of frequency, see Fig. 2(a). In the  $b_0 / \mu \ll 1$  and  $\omega / \mu \ll 1$  limit, we find

$$\text{Re} \Pi_L(\omega, p) \approx \frac{2\mu b_0 \alpha^2}{\pi^2} \left( 1 - \frac{\omega^2}{12\mu^2 \alpha^2} \right), \quad (6)$$

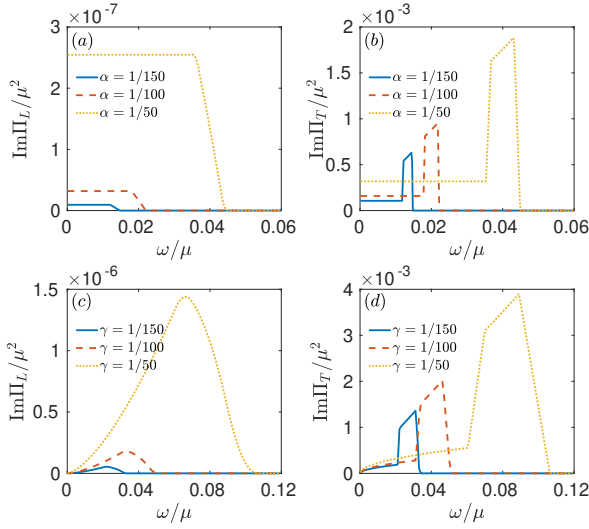


FIG. 1. The imaginary parts of the longitudinal and transverse response functions for  $\omega = v_s p \equiv \alpha v_F p$  [(a)-(b)] and  $\omega = D p^2 \equiv \gamma v_F / k_F p^2$  [(c)-(d)]. Here we take the chemical  $\mu$  and Fermi velocity  $v_F$  to be unity and  $b_0$  is fixed to be 0.1 $\mu$ .

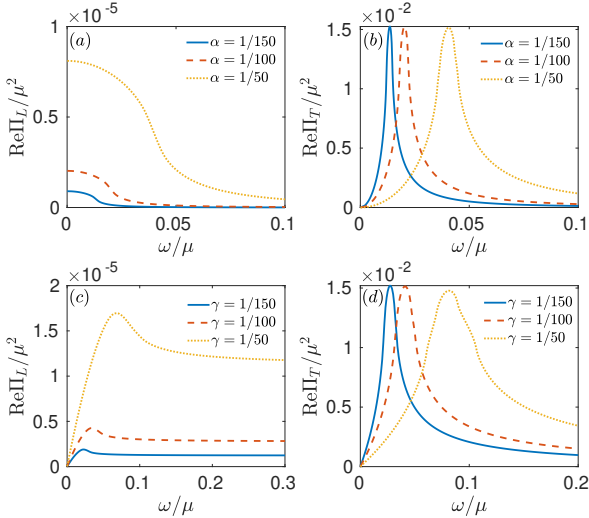


FIG. 2. The real parts of the longitudinal and transverse response functions for linear [(a)-(b)] and quadratic [(c)-(d)] dispersion relations. Other parameters are the same as in Fig. 1. The peaks in (b) and (d) are located at  $\omega \sim 2\alpha\mu$  and  $\omega \sim 4\gamma\mu$ , respectively.

which is nonvanishing in the zero frequency limit. In the large  $\omega$  limit,

$$\text{Re}\Pi_L(\omega, p) \approx \frac{8\mu b_0(\mu^2 + b_0^2)\alpha^4}{3\pi^2} \frac{1}{\omega^2}, \quad (7)$$

which decreases as  $1/\omega^2$  and is suppressed by  $v_F^4/v_s^4$ .

In contrast to the longitudinal counterpart, the real part of the transverse response function first increases with increasing  $\omega$  and then decreases after reaching a

maximum, see Fig. 2(b). In the small  $\omega$  and  $b_0$  limit,

$$\text{Re}\Pi_T(\omega, p) \approx -\frac{2\mu b_0 \alpha^2}{\pi^2} \left(1 - \frac{\omega^2}{12\mu^2 \alpha^4}\right), \quad (8)$$

which is also nonzero in the  $\omega \rightarrow 0$  limit but takes the opposite value compared to the longitudinal response. One may expect that, in the long wave length limit, the electrons cannot distinguish between the transverse and longitudinal waves, resulting in identical responses. This holds true if the frequency remains finite as the momentum approaches to zero; in our situation, however, both  $\omega$  and  $p$  approach to zero, and since  $v_F p \gg \omega$ , the momentum transfer cannot be ignored and the system responds to longitudinal and transverse waves in different manners even in the zero frequency and momentum limit.

In the large  $\omega$  limit, the real part of the transverse response is

$$\text{Re}\Pi_T(\omega, p) \approx \frac{8\mu b_0(\mu^2 + b_0^2)\alpha^2}{3\pi^2} \frac{1}{\omega^2}, \quad (9)$$

which decreases as  $1/\omega^2$  and is suppressed by  $v_F^2/v_s^2$ . From the low and high frequency expansions Eqs. (8) and (9), we can estimate that the position of the peak of  $\text{Re}\Pi_T$  locates at  $\omega \sim 2\alpha\mu$ . The height of the peak can be estimated as  $4\mu b_0/(3\pi^2)$ , which agrees very well with numerical results. Note that the height of the peak is not suppressed by  $v_F/v_s$ , and therefore the transverse response can be much larger than the longitudinal one.

Physically, the peak appears because, when the momentum of the axial gauge field is about  $\mathbf{p} \approx -2\mathbf{k}_F$ , electrons can be back scattered to the same Fermi surface. This Fermi surface nesting effect leads to a large phase space that is responsible for the enhancement of the transverse response function. Due to the spin-momentum locking of Weyl fermions, the longitudinal transition amplitude is vanishingly small if  $\mathbf{p} \sim -2\mathbf{k}_F$ . Consequently, no peak is observed in the longitudinal response function for the linear dispersion relation case. However, as we will demonstrate subsequently, the longitudinal response also manifests a peak around  $p \approx 2k_F$  for external perturbations with quadratic dispersion.

The results for the quadratic dispersion relation are shown in Fig. 2(c)-(d). Different from the linear dispersion case, the real parts of the response functions in the small frequency limit are now proportional to  $\omega$ ,

$$\text{Re}\Pi_L(\omega, p) \approx \frac{2\gamma b_0}{\pi^2} \omega, \quad (10)$$

and

$$\text{Re}\Pi_T(\omega, p) \approx \frac{b_0}{6\pi^2 \gamma} \omega. \quad (11)$$

Note that with the increasing of frequency, the transverse response increases much faster than the longitudinal one. In the large frequency limit, we find that the longitudinal response approaches to a constant

$$\text{Re}\Pi_L(\omega, p) \approx \frac{8\mu b_0 \gamma^2}{3\pi^2} + \frac{32\gamma^3 \mu^2 b_0}{15\pi^2 \omega}, \quad (12)$$

and the transverse one decays as  $1/\omega$

$$\text{Re}\Pi_T(\omega, p) \approx \frac{8\gamma\mu^2 b_0}{3\pi^2\omega}. \quad (13)$$

As can be seen in Fig. 2(d), for the transverse response

$$\text{Re}\Pi_H^{\text{intra}}(\omega, p) = \sum_{\lambda} \lambda \theta(p - |\omega|) \theta(2\mu_{\lambda} - \omega - p) F_H(\omega, \mu_{\lambda}, p) - (\omega \rightarrow -\omega) - (\mu \rightarrow -\mu), \quad (14)$$

$$\text{Re}\Pi_H^{\text{inter}}(\omega, p) = \sum_{\lambda} \lambda \theta(|\omega| - p) \theta(p - |\omega + 2\mu_{\lambda}|) F_H(-\omega, \mu_{\lambda}, p) - (\omega \rightarrow -\omega), \quad (15)$$

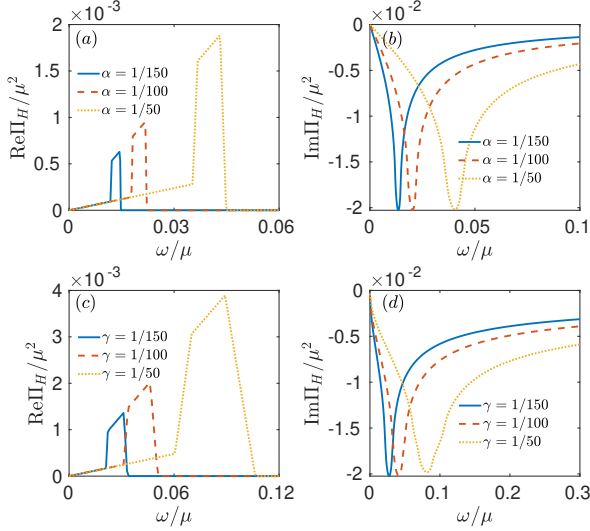


FIG. 3. The real and imaginary parts of the off-diagonal response functions for linear [(a)-(b)] and quadratic [(c)-(d)] dispersion relations. Other parameters are the same as in Fig. 1. The peaks in (b) and (d) are located at  $\omega \sim 2\alpha\mu$  and  $\omega \sim 4\gamma\mu$ , respectively.

where  $F_H(\omega, \mu, p) = (p^2 - \omega^2)[p^2 - (\omega - 2\mu)^2]/(64\pi p^2)$ . The imaginary part is obtained through the Kramers-Kronig relation. Since the real part of the Hall response is odd in frequency, the imaginary part is even.

In Fig. 3 we plot the off-diagonal response  $\Pi_{xy}^H$  for linear [(a)-(b)] and quadratic dispersions [(c)-(d)] as functions of frequency, and one can see that the response functions show similar features for both cases. In the small frequency limit, the real part increases linearly with frequency and the step function feature is observed with further increasing  $\omega$ . The real part is typically smaller than the imaginary part, so in the following we focus on the latter.

For the linear dispersion case and in the small  $\omega$  limit, the imaginary part of the response function increases lin-

early with  $\omega$ , there is a peak located at  $\omega \sim 4\gamma\mu$ , and the height of the peak can be estimated as  $4\mu b_0/(3\pi^2)$ , which is independent of  $\gamma$ . The longitudinal response also exhibits a peak, see Fig. 2(c), and the height of the peak is about  $4\mu b_0\gamma^2/\pi^2$ , which is suppressed by  $\gamma^2$ .

*Hall response.*— We now study the Hall response  $\Pi_H(\omega, p)$ . It is convenient to first compute the real part,

early with  $\omega$ ,

$$\text{Im}\Pi_H(\omega, p) \approx -\frac{b_0\omega}{2\pi^2\alpha}, \quad (16)$$

while for large  $\omega$ , it decays as  $1/\omega$ ,

$$\text{Im}\Pi_H(\omega, p) \approx -\frac{2\alpha\mu^2 b_0}{\pi^2\omega}, \quad (17)$$

so the response function reaches a maximal magnitude  $2\mu b_0/\pi^2$  at  $\omega \approx 2\alpha\mu$ , which is similar to the diagonal transverse response function.

For the quadratic dispersion relation, we find that the response function increases as  $\sqrt{\omega}$  in the small frequency limit,

$$\text{Im}\Pi_H(\omega, p) \approx -\frac{b_0\sqrt{\mu\omega/\gamma}}{2\pi^2}, \quad (18)$$

and in the large frequency limit,

$$\text{Im}\Pi_H(\omega, p) \approx -\frac{2b_0\sqrt{\mu^3\gamma}}{\pi^2\sqrt{\omega}}, \quad (19)$$

which decays as  $1/\sqrt{\omega}$ . So around  $\omega \sim 4\gamma\mu$ , it manifests a peak with the magnitude about  $2b_0\mu/\pi^2$ .

Similar to the transverse response function, the magnitude of the peak for the Hall response function is determined by the properties of Weyl fermions and is independent of  $\alpha$  or  $\gamma$ .

*Effects of disorder.*— To explore the effects of disorder, we replace the clean limit Matsubara Green's function by [52]  $G(i\omega_n, \mathbf{k}) = [i\omega_n - H(\mathbf{k}) - \mu + i\Gamma\text{sign}(\omega_n)]^{-1}$ , where  $\Gamma$  is a constant scattering rate. We focus on the transverse and Hall responses, as they are large in the clean limit.

Figure 4 shows the results for several different disorder strengths  $\Gamma$  at fixed  $\alpha$ . As shown in panels (a) and (d), the step-like feature can be observed for small  $\Gamma$  and diminishes gradually as  $\Gamma$  increases. However, the peaks are quite robust even for relatively large  $\Gamma$ , see Fig. 4(b) and (c). Notably, the peak positions are barely

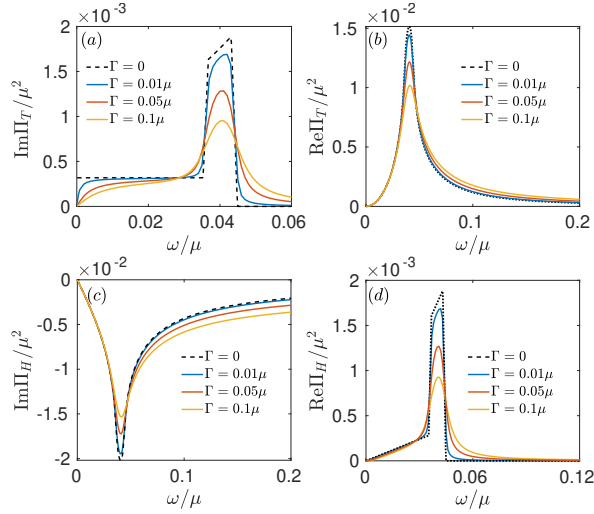


FIG. 4. The transverse [(a)-(b)] and Hall [(c)-(d)] response functions in the presence of disorder for the linear dispersion with  $\alpha = 1/50$  and  $b_0 = 0.1\mu$ .

changed compared to the clean limit values. We have also performed calculations for quadratic dispersion and observed qualitatively similar behavior.

*Application I: Hall type magnetopiezoelectric effect.*— Recently, in metals that break both time-reversal and inversion symmetries, a new type of piezoelectricity, the dynamical magnetopiezoelectric effect has been introduced [46–48] and observed [49]. As an application of our results, we here propose that time-reversal and inversion breaking Weyl semimetals show a Hall type magnetopiezoelectric effect, where an electric current is induced by transverse sound wave, and the direction of the current is perpendicular to the directions of sound propagation and polarization.

Following [53], strain in Weyl semimetals is related to the axial gauge field as  $A_{5,i} = bu_{iz} + b\delta_{iz}\sum_j u_{jj}$ , here we have assumed that the Weyl nodes are separated along the  $z$ -direction, but the expression can be extended to other directions of Weyl nodes separation. The strain tensor is  $u_{ij} = (\partial_i u_j + \partial_j u_i)/2$  with  $\mathbf{u}(t, \mathbf{r})$  being the displacement field. As an example, we consider a transverse sound wave propagating in the  $z$ -direction,  $\mathbf{u} = u_0 \mathbf{e}_x e^{i(qz - \omega t)}$ . Then the induced axial gauge field  $A_{5,x} \approx iqb u_0 e^{i(qz - \omega t)}$  can induce an electric current in the  $y$  direction. The Fourier transform of the electric current in the low frequency limit is  $j_y = eb_0 b q^2 u_0 / (2\pi^2 \hbar)$ , where we have recovered  $\hbar$  and electric charge  $-e$ . In noncentrosymmetric magnetic Weyl semimetals, the Weyl node separation in the momentum space  $b$  is of the order of  $0.1 \times 2\pi/a$  with  $a$  being the lattice constant, and  $b_0$  is of the order of meV [39]. Assuming that the displacement field  $u_0$  is about one

percent of the lattice constant and the sound velocity is of the order of  $10^5 \text{ cm/s}$ , then the induced current is estimated as

$$j_y \approx 0.3 \left( \frac{\omega}{2\pi \text{ MHz}} \right)^2 \frac{\mu \text{ A}}{\text{cm}^2}. \quad (20)$$

Our order of magnitude estimate indicates that the effect is large enough to be detected.

*Application II: Magnon and electric field interconversion.*— The creation and manipulation of magnons are the central focus of magnon spintronics [54]. Our results provide a possible mechanism to excite magnons in noncentrosymmetric magnetic Weyls. In these materials, local moments couple to Weyl fermions through  $K \mathbf{m}(\mathbf{r}) \cdot \mathbf{s}$ , where  $K$  is the Kondo coupling constant,  $\mathbf{m}$  is the local moments, and  $\mathbf{s}$  is the spin operator of Weyl fermions [43, 55]. The spin and pseudospin are generally different and their connection is material-dependent. For simplicity, we assume they are identical [43, 55]. Under this approximation, the magnetization  $\mathbf{m}$  becomes proportional to the axial gauge potential  $\mathbf{A}_5$  [11, 56] when expanding the Kondo interaction around the Weyl nodes. Thus according to our main results, spin waves can induce electric currents in noncentrosymmetric magnetic Weyl semimetals. This in turn provides a way to excite magnons using electric fields, which is similar to the inverse magnetopiezoelectric effect [47]. The transverse response function reaches a maximal around  $\omega \sim \alpha\mu$  or  $\omega \sim \gamma\mu$ . Light with frequencies near  $\gamma\mu$  or  $\alpha\mu$  could therefore be used to excite magnons; however, further research is required to establish viable experimental setups.

*Conclusion.*— We investigate the electric current induced by axial gauge fields in time-reversal and inversion breaking Weyl semimetals. We calculate the longitudinal, transverse, and Hall type response functions for both linear and quadratic dispersion relations of axial gauge potentials. We find that the transverse and Hall responses are much larger than the longitudinal one. With increasing frequency, the transverse and Hall response functions manifest a peak whose height is determined by the parameters of Weyl fermions and is independent of external perturbations. We additionally demonstrate that the essential features of the response functions survive in the presence of disorder. As applications of our results, we predict a Hall type magnetopiezoelectric effect, where a sizable electric current can be generated by dynamical strain. Additionally, we propose a possible mechanism to excite magnons using electric fields in noncentrosymmetric magnetic Weyl semimetals and this could be exploited for magnon spintronics.

*Acknowledgments.*— We thank P. O. Sukhachov and Xi Luo for useful discussions. This work is supported by National Natural Science Foundation of China (Grant No. 12204329).



- 
- [1] N. P. Armitage, E. J. Mele, and A. Vishwanath, Weyl and Dirac semimetals in three-dimensional solids, *Rev. Mod. Phys.* **90**, 015001 (2018).
- [2] B. Q. Lv, T. Qian, and H. Ding, Experimental perspective on three-dimensional topological semimetals, *Rev. Mod. Phys.* **93**, 025002 (2021).
- [3] R. Ilan, A. G. Grushin, and D. I. Pikulin, Pseudo-electromagnetic fields in 3D topological semimetals, *Nat. Rev. Phys.* **2**, 29 (2020).
- [4] J. Yu and C.-X. Liu, Pseudo-gauge fields in Dirac and Weyl materials, in *Topological Insulator and Related Topics* (Elsevier, 2021) p. 195–224.
- [5] M. M. Jadidi, M. Kargarian, M. Mittendorff, Y. Aytac, B. Shen, J. C. König-Otto, S. Winnerl, N. Ni, A. L. Gaeta, T. E. Murphy, and H. D. Drew, Nonlinear optical control of chiral charge pumping in a topological Weyl semimetal, *Phys. Rev. B* **102**, 245123 (2020).
- [6] S. Nandy and D. A. Pesin, Chiral magnetic effect of hot electrons, *Phys. Rev. Lett.* **125**, 266601 (2020).
- [7] Z. Song, J. Zhao, Z. Fang, and X. Dai, Detecting the chiral magnetic effect by lattice dynamics in Weyl semimetals, *Phys. Rev. B* **94**, 214306 (2016).
- [8] X. Yuan, C. Zhang, Y. Zhang, Z. Yan, T. Lyu, M. Zhang, Z. Li, C. Song, M. Zhao, P. Leng, M. Ozerov, X. Chen, N. Wang, Y. Shi, H. Yan, and F. Xiu, The discovery of dynamic chiral anomaly in a Weyl semimetal NbAs, *Nat. Commun.* **11**, 1259 (2020).
- [9] A. Cortijo, D. Kharzeev, K. Landsteiner, and M. A. H. Vozmediano, Strain-induced chiral magnetic effect in Weyl semimetals, *Phys. Rev. B* **94**, 241405 (2016).
- [10] J. Diaz, C. Putzke, X. Huang, A. Estry, J. G. Analytis, D. Sabsovich, A. G. Grushin, R. Ilan, and P. J. W. Moll, Bending strain in 3D topological semi-metals, *J. Phys. D: Appl. Phys.* **55**, 084001 (2021).
- [11] A. A. Zyuzin, S. Wu, and A. A. Burkov, Weyl semimetal with broken time reversal and inversion symmetries, *Phys. Rev. B* **85**, 165110 (2012).
- [12] D. T. Son and N. Yamamoto, Berry curvature, triangle anomalies, and the chiral magnetic effect in Fermi liquids, *Phys. Rev. Lett.* **109**, 181602 (2012).
- [13] J.-H. Zhou, H. Jiang, Q. Niu, and J.-R. Shi, Topological invariants of metals and the related physical effects, *Chin. Phys. Lett.* **30**, 027101 (2013).
- [14] P. E. C. Ashby and J. P. Carbotte, Magneto-optical conductivity of Weyl semimetals, *Phys. Rev. B* **87**, 245131 (2013).
- [15] C. J. Tabert and J. P. Carbotte, Optical conductivity of Weyl semimetals and signatures of the gapped semimetal phase transition, *Phys. Rev. B* **93**, 085442 (2016).
- [16] J. P. Carbotte, Dirac cone tilt on interband optical background of type-I and type-II Weyl semimetals, *Phys. Rev. B* **94**, 165111 (2016).
- [17] B. Roy and V. Juričić, Optical conductivity of an interacting Weyl liquid in the collisionless regime, *Phys. Rev. B* **96**, 155117 (2017).
- [18] M. Stålhammar, J. Larana-Aragon, J. Knolle, and E. J. Bergholtz, Magneto-optical conductivity in generic Weyl semimetals, *Phys. Rev. B* **102**, 235134 (2020).
- [19] S. Acheche, R. Nourafkan, J. Padayasi, N. Martin, and A.-M. S. Tremblay, Interaction and temperature effects on the magneto-optical conductivity of Weyl liquids, *Phys. Rev. B* **102**, 045148 (2020).
- [20] J.-T. Hou, C.-X. Yan, C.-Y. Tan, Z.-Q. Li, P. Wang, H. Guo, and H.-R. Chang, Effects of spatial dimensionality and band tilting on the longitudinal optical conductivities in Dirac bands, *Phys. Rev. B* **108**, 035407 (2023).
- [21] S. P. Mukherjee and J. P. Carbotte, Imaginary part of Hall conductivity in a tilted doped weyl semimetal with both broken time-reversal and inversion symmetry, *Phys. Rev. B* **97**, 035144 (2018).
- [22] A. Cortijo, D. Kharzeev, K. Landsteiner, and M. A. H. Vozmediano, Strain-induced chiral magnetic effect in Weyl semimetals, *Phys. Rev. B* **94**, 241405 (2016).
- [23] D. I. Pikulin, A. Chen, and M. Franz, Chiral anomaly from strain-induced gauge fields in Dirac and Weyl semimetals, *Phys. Rev. X* **6**, 041021 (2016).
- [24] A. G. Grushin, J. W. Venderbos, A. Vishwanath, and R. Ilan, Inhomogeneous Weyl and Dirac semimetals: Transport in axial magnetic fields and Fermi arc surface states from pseudo-Landau levels, *Phys. Rev. X* **6**, 041046 (2016).
- [25] K. Landsteiner, Notes on anomaly induced transport, *Acta Phys. Pol. B* **47**, 2617 (2016).
- [26] Z.-M. Huang, J. Zhou, and S.-Q. Shen, Topological responses from chiral anomaly in multi-Weyl semimetals, *Phys. Rev. B* **96**, 085201 (2017).
- [27] A. Westström and T. Ojanen, Designer curved-space geometry for relativistic fermions in Weyl metamaterials, *Phys. Rev. X* **7**, 041026 (2017).
- [28] M. N. Chernodub and M. A. Zubkov, Chiral anomaly in Dirac semimetals due to dislocations, *Phys. Rev. B* **95**, 115410 (2017).
- [29] P. O. Sukhachov and H. Rostami, Acousto-galvanic effect in Dirac and Weyl semimetals, *Phys. Rev. Lett.* **124**, 126602 (2020).
- [30] L. Liang and T. Ojanen, Topological magnetotorsional effect in weyl semimetals, *Phys. Rev. Res.* **2**, 022016 (2020).
- [31] S. Ghosh, D. Sinha, S. Nandy, and A. Taraphder, Chirality-dependent planar Hall effect in inhomogeneous Weyl semimetals, *Phys. Rev. B* **102**, 121105 (2020).
- [32] J. D. Hannukainen, Y. Ferreira, A. Cortijo, and J. H. Bardarson, Axial anomaly generation by domain wall motion in Weyl semimetals, *Phys. Rev. B* **102**, 241401(R) (2020).
- [33] L. Liang, P. O. Sukhachov, and A. V. Balatsky, Axial magnetoelectric effect in Dirac semimetals, *Phys. Rev. Lett.* **126**, 247202 (2021).
- [34] A. A. Herasymchuk, P. O. Sukhachov, and E. V. Gorbar, Electric and chiral response to a pseudoelectric field in Weyl materials, *Phys. Rev. B* **106**, 045132 (2022).
- [35] L. Liang, Anomalous chiral magnetic effect in time reversal symmetry breaking Weyl semimetals, *Phys. Rev. B* **107**, 125101 (2023).
- [36] W. Shi, L. Muechler, K. Manna, Y. Zhang, K. Koepernik, R. Car, J. van den Brink, C. Felser, and Y. Sun, Prediction of a magnetic Weyl semimetal without spin-orbit coupling and strong anomalous Hall effect in the Heusler compensated ferrimagnet  $\text{Ti}_2\text{MnAl}$ , *Phys. Rev. B* **97**, 060406 (2018).
- [37] J. Noky, J. Gayles, C. Felser, and Y. Sun, Strong

- anomalous Nernst effect in collinear magnetic Weyl semimetals without net magnetic moments, *Phys. Rev. B* **97**, 220405 (2018).
- [38] D. Grassano, L. Binci, and N. Marzari, Type-I antiferromagnetic Weyl semimetal  $\text{InMnTi}_2$ , *Phys. Rev. Res.* **6**, 013140 (2024).
- [39] G. Chang, B. Singh, S.-Y. Xu, G. Bian, S.-M. Huang, C.-H. Hsu, I. Belopolski, N. Alidoust, D. S. Sanchez, H. Zheng, H. Lu, X. Zhang, Y. Bian, T.-R. Chang, H.-T. Jeng, A. Bansil, H. Hsu, S. Jia, T. Neupert, H. Lin, and M. Z. Hasan, Magnetic and noncentrosymmetric Weyl fermion semimetals in the  $\text{RAlGe}$  family of compounds ( $\text{R}=\text{rare earth}$ ), *Phys. Rev. B* **97**, 041104 (2018).
- [40] D. S. Sanchez, G. Chang, I. Belopolski, H. Lu, J.-X. Yin, N. Alidoust, X. Xu, T. A. Cochran, X. Zhang, Y. Bian, S. S. Zhang, Y.-Y. Liu, J. Ma, G. Bian, H. Lin, S.-Y. Xu, S. Jia, and M. Z. Hasan, Observation of Weyl fermions in a magnetic non-centrosymmetric crystal, *Nat. Commun.* **11**, 3356 (2020).
- [41] J. Gaudet, H.-Y. Yang, S. Baidya, B. Lu, G. Xu, Y. Zhao, J. A. Rodriguez-Rivera, C. M. Hoffmann, D. E. Graf, D. H. Torchinsky, P. Nikolić, D. Vanderbilt, F. Tafti, and C. L. Broholm, Weyl-mediated helical magnetism in  $\text{NdAlSi}$ , *Nat. Mater.* **20**, 1650 (2021).
- [42] X. Yao, J. Gaudet, R. Verma, D. E. Graf, H.-Y. Yang, F. Bahrami, R. Zhang, A. A. Aczel, S. Subedi, D. H. Torchinsky, J. Sun, A. Bansil, S.-M. Huang, B. Singh, P. Blaha, P. Nikolić, and F. Tafti, Large topological Hall effect and spiral magnetic order in the Weyl semimetal  $\text{SmAlSi}$ , *Phys. Rev. X* **13**, 011035 (2023).
- [43] N. C. Drucker, T. Nguyen, F. Han, P. Siriviboon, X. Luo, N. Andrejevic, Z. Zhu, G. Bednik, Q. T. Nguyen, Z. Chen, L. K. Nguyen, T. Liu, T. J. Williams, M. B. Stone, A. I. Kolesnikov, S. Chi, J. Fernandez-Baca, C. S. Nelson, A. Alatas, T. Hogan, A. A. Puretzky, S. Huang, Y. Yu, and M. Li, Topology stabilized fluctuations in a magnetic nodal semimetal, *Nat. Commun.* **14**, 5182 (2023).
- [44] A. Laha, A. K. Kundu, N. Aryal, E. S. Bozin, J. Yao, S. Paone, A. Rajapitamahuni, E. Vescovo, T. Valla, M. Abeykoon, R. Jing, W. Yin, A. N. Pasupathy, M. Liu, and Q. Li, Electronic structure and magnetic and transport properties of antiferromagnetic Weyl semimetal  $\text{GdAlSi}$ , *Phys. Rev. B* **109**, 035120 (2024).
- [45] J. Kunze, M. Köpf, W. Cao, Y. Qi, and C. A. Kuntscher, Optical signatures of type-II Weyl fermions in the non-centrosymmetric semimetals  $\text{RAlSi}$  ( $\text{R}=\text{La, Ce, Pr, Nd, Sm}$ ), *Phys. Rev. B* **109**, 195130 (2024).
- [46] D. Varjas, A. G. Grushin, R. Ilan, and J. E. Moore, Dynamical piezoelectric and magnetopiezoelectric effects in polar metals from Berry phases and orbital moments, *Phys. Rev. Lett.* **117**, 257601 (2016).
- [47] H. Watanabe and Y. Yanase, Magnetic hexadecapole order and magnetopiezoelectric metal state in  $\text{Ba}_{1-x}\text{K}_x\text{Mn}_2\text{As}_2$ , *Phys. Rev. B* **96**, 064432 (2017).
- [48] P. Rodriguez-Lopez and A. Cortijo, Theory of the strain-induced magnetoelectric effect in planar Dirac systems, *Phys. Rev. B* **97**, 235128 (2018).
- [49] Y. Shiomi, H. Watanabe, H. Masuda, H. Takahashi, Y. Yanase, and S. Ishiwata, Observation of a magnetopiezoelectric effect in the antiferromagnetic metal  $\text{EuMnBi}_2$ , *Phys. Rev. Lett.* **122**, 127207 (2019).
- [50] D. Belitz, T. R. Kirkpatrick, and A. Rosch, Theory of helimagnons in itinerant quantum systems, *Phys. Rev. B* **73**, 054431 (2006).
- [51] The Fermi velocity  $v_F$  of Weyl semimetals is of the order of  $10^6\text{m/s}$ , while the sound velocity  $v_s$  is of the order of  $10^3\text{m/s}$ , so  $\alpha = v_s/v_F \ll 1$ . The spin stiffness  $D$  is typically of the order of  $\text{meV}\text{\AA}^2$ , while  $\hbar v_F$  is of the order of  $\text{eV}\text{\AA}$  and the Fermi momentum  $k_F$  is of the order of  $\text{\AA}^{-1}$ , thus  $\gamma = Dk_F/v_F \ll 1$ .
- [52] A. Altland and B. D. Simons, *Condensed Matter Field Theory*, 2nd ed. (Cambridge University Press, 2010).
- [53] A. Cortijo, Y. Ferreirós, K. Landsteiner, and M. A. H. Vozmediano, Elastic gauge fields in Weyl semimetals, *Phys. Rev. Lett.* **115**, 177202 (2015).
- [54] A. V. Chumak, V. I. Vasyuchka, A. A. Serga, and B. Hillebrands, Magnon spintronics, *Nat. Phys.* **11**, 453 (2015).
- [55] H.-R. Chang, J. Zhou, S.-X. Wang, W.-Y. Shan, and D. Xiao, RKKY interaction of magnetic impurities in Dirac and Weyl semimetals, *Phys. Rev. B* **92**, 241103 (2015).
- [56] A. A. Burkov, M. D. Hook, and L. Balents, Topological nodal semimetals, *Phys. Rev. B* **84**, 235126 (2011).